Supporting Information

Hybridized Guided-Mode Resonances *via* Colloidal Plasmonic Self-Assembled Grating

Swagato Sarkar,[1,2] Vaibhav Gupta,[1] Mohit Kumar,[1,2] Jonas Schubert,[1] Patrick T. Probst,[1] Joby Joseph,[2] Tobias A.F. König[1,3,*]

[1]Leibniz-Institut für Polymerforschung Dresden e.V. (IPF), Institute for Physical Chemistry and Polymer Physics, Hohe Str. 6, 01069 Dresden, Germany
[2]Photonics Research Lab, Department of Physics, Indian Institute of Technology Delhi, New Delhi, 110016, India
[3]Cluster of Excellence Center for Advancing Electronics Dresden (cfaed), Technische Universität Dresden, 01062 Dresden, Germany

*Corresponding e-mail: koenig@ipfdd.de

T1: Optical constants of TiO_2, ma-N 405 photoresist and glass substrate measured from spectroscopic ellipsometry

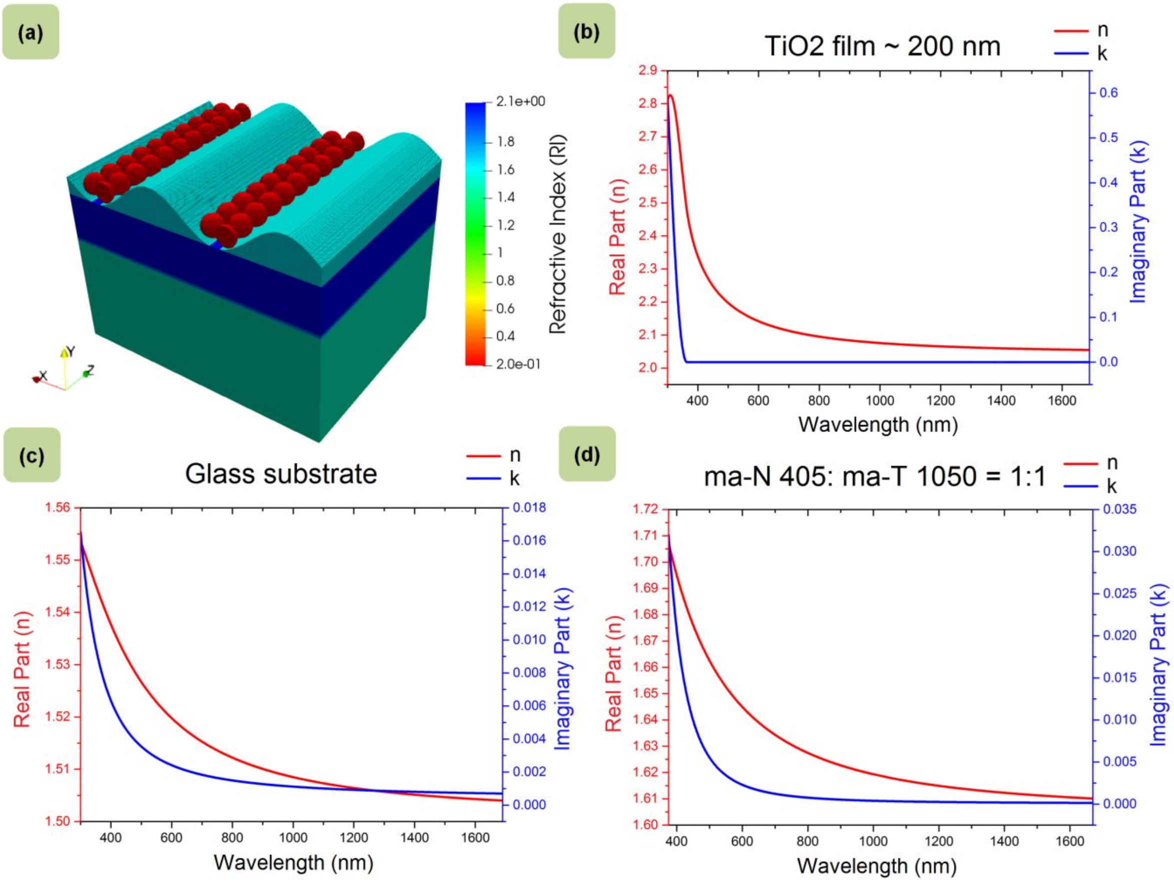

FigureS1 | Measured refractive index data used for FDTD simulations: (a) 3D index data of the hybrid structure observed at λ = 851 nm. (b), (c) and (d) Real and imaginary values of the refractive index data of TiO_2, glass, and diluted photoresist respectively measured through spectroscopic ellipsometer and included in the simulation model.

Figure S1 (a) shows the refractive index profile of the hybrid structure at 851 nm with optical constant data fitted from experimentally measured values using spectroscopic ellipsometry (RC2-DI, J.A. Woollam Co., Inc.). Thin films of TiO_2 and diluted photoresist along with bare glass substrate are separately measured for the entire range of operation (400-2400 nm) and plotted in Figure S1 (b-d). These data are incorporated in the Lumerical software to provide proper materialist properties to the designed models that are used throughout the article for comparative analysis of different resonance mechanisms.

T2: Concepts of a guided-mode resonant (GMR) structure

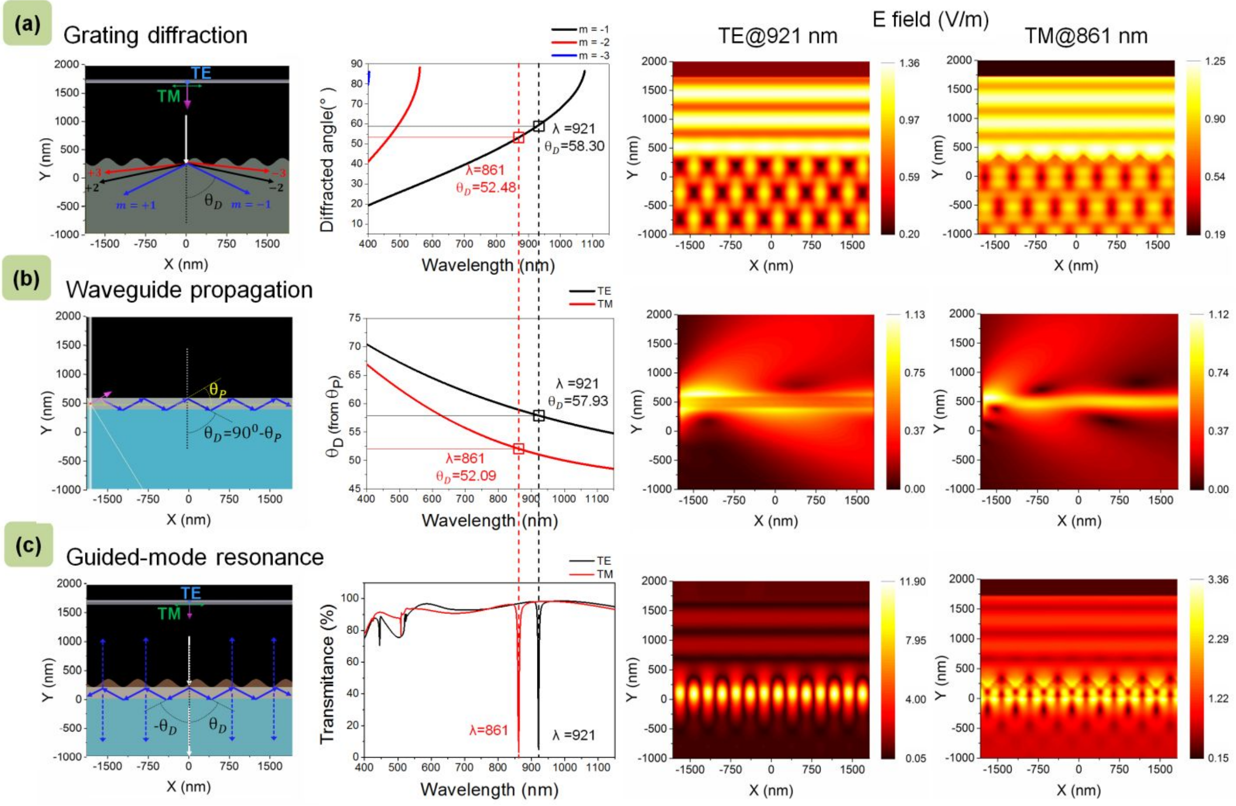

FigureS2 | Physical interpretation of Guided-Mode Resonance (GMR) in terms of its building blocks: (a) Schematic of grating diffraction for a period of 520 nm. The plot shows diffracted angle vs wavelength for different transmission orders (b) Ray picture of waveguide propagation with propagating angle θ_P inside a slab waveguide. Plot shows θ_D (from θ_P) for TE and TM as a function of wavelength with a fixed waveguide thickness and constituting index. (c) GMR as grating plus waveguide structure. Ray picture shows diffraction leading to the propagation and coupling out. Destructive interference of these leaked out orders with zeroth order produce sharp transmission dips at 921and 861nm for the TE and TM case respectively. Electric field $\left(|\vec{E}|\right)$ profiles at 921 and 861 nm are shown in (a), (b), and (c) showing diffraction of orders, waveguiding and strong resonance within waveguide correspondingly.

Figure S2 explains the working principle of a guided mode resonant (GMR) structure. The left column exhibits the geometrical representations of a GMR structure and its building blocks, the grating and the waveguide. The dimensions of these structures are matched to the electric field $\left(|\vec{E}|\right)$ profiles to the right (third and fourth) to correlate the spatial distribution within these geometries. Figure S2 (a) exhibits a sinusoidal grating of higher index $n_2 = n_{TiO2}$, backed by a lower index of $(n_1 = n_{air} = 1.00)$. The plot explains how the diffraction first order angle in transmission depends on wavelength for a fixed period of 520 nm and for normal incidence $(\theta_{inc} = 0°)$. This is quite straightforward and comes from the polarization independent grating equation

$$n_2 \sin\theta_D(m) = n_1 \sin\theta_{inc} - m\frac{\lambda}{\Lambda} \tag{1}$$

In Figure S2 (b), a waveguide of thickness 200 nm and index $n_2 = n_{TiO2}$ is associated with lower indexed superstrate $n_1 = (n_{pr} + n_{air})/2$ and substrate $n_3 = n_{glass}$. The indices n_{TiO2}, n_{pr}, and n_{glass} are wavelength dependent properties of titanium dioxide, photoresist, and glass respectively, measured through spectroscopic ellipsometry and given in Figure S1. The graph shows a plot of different propagation angle (θ_P) for different wavelengths expressed in terms of different diffracted angles $(\theta_D = 90° - \theta_P)$ for the cases of transverse electric (TE) and transverse magnetic (TM) modes. These propagation angles are directly related to the wavelength dependent n_{eff} of the waveguide and can be calculated via numerical methods. Figure S2 (c) shows the GMR structure interpreted as a grating together with a slab waveguide with n_{pr}, n_{TiO2}, and n_{glass} as grating, waveguide, and substrate indices. For a grating to decide the wavelength dependent diffraction angle (θ_D) that leads to propagation angle $(\theta_P = 90° - \theta_D)$; only specific wavelengths depending on the polarization can produce these θ_P supported for the combined structure. As seen from the plots, the wavelength at 921 nm for TE mode only can give a diffraction angle of 58.3°as well as a propagating condition relating to θ_D of 57.93° within this waveguide structure. The similar cases arise for the TM mode at 861 nm that satisfies both the case of diffraction and waveguiding for $\theta_D \sim 52°$. While propagating within the waveguide these selective wavelengths (TE and TM) interacts with the gratings to diffract out and destructively interfere with the corresponding wavelength of the zeroth order transmission. These result in sharp GMR transmission dips as seen in Figure S2 (c). The Electric field $\left(|\vec{\boldsymbol{E}}|\right)$ profiles for the TE 921nm and TM 861 nm are shown in the right columns (third and fourth) corresponding to these individual cases and are described here. Figure S2 (a) explains diffraction of a plane wave source upon encountering a high indexed sinusoidal gating. The modulussquare of these orders at far-field can superpose to produce the well-known grating diffraction intensity pattern. Figure S2 (b) depicts a cross-section of the angled-injection case for waveguiding of fundamental TE and TM modes. Figure S2 (c) represents the case of guided-mode resonance within the waveguide with highly intensified electric fields as seen from the associated color bars. These modes can be interpreted as standing waves formed due to the interference of two counter-propagating diffracted waves referred to as the '+1' and '-1' orders

T3: Laser Interference Lithography using Lloyd's mirror setup

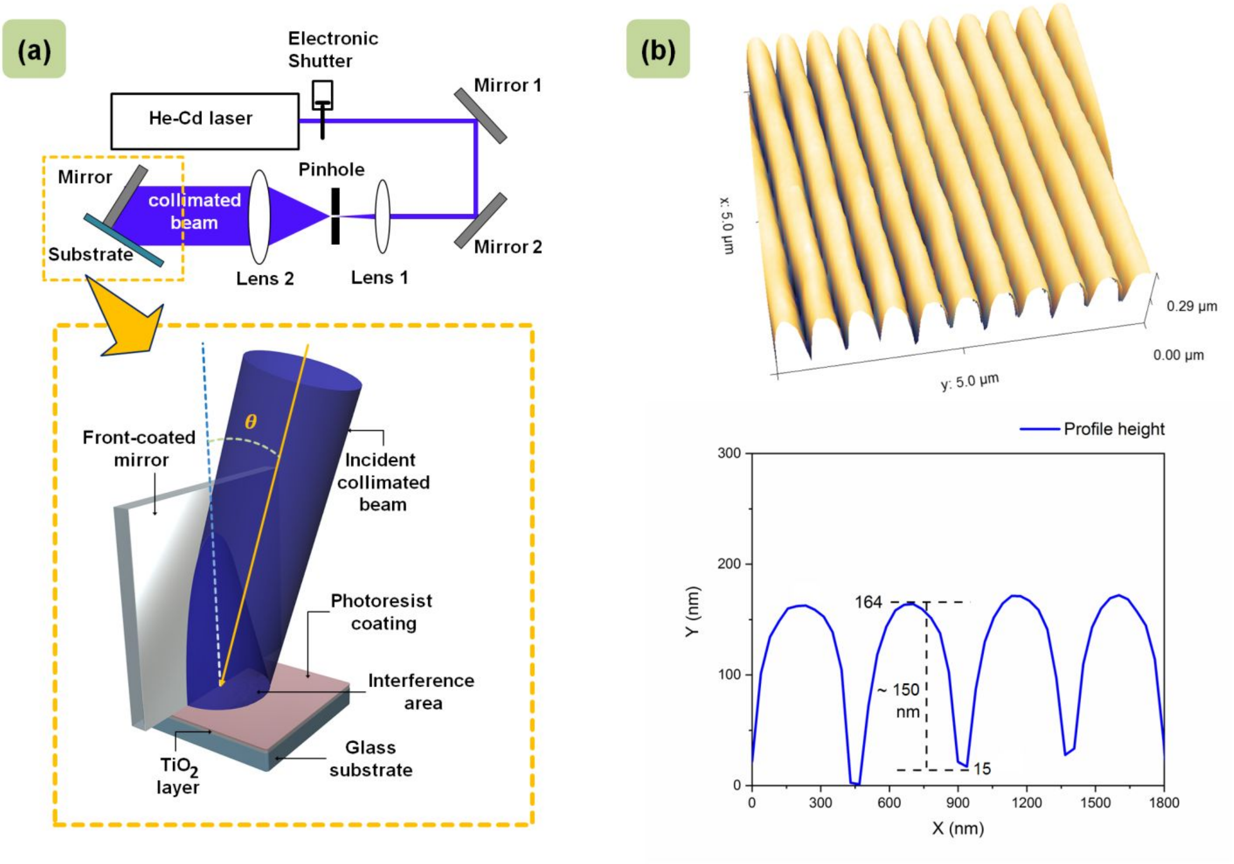

FigureS3 | Fabrication and AFM characterization of a 1D grating structure on photoresist: (a) Experimental setup for Lloyd mirror-based laser interference lithography (LIL). (b) AFM image of a periodic grating on photoresist obtained through LIL. Height profile of the observed grating is also provided.

Figure S3 (a) shows the experimental setup for the fabrication of periodic structures using Lloyd Mirror based laser interference lithography. A 325 nm He-Cd laser (Kimmon-Koha, Japan) is spatially filtered using lens and pinhole arrangement and further collimated using another lens. The collimated beam is incident on the sample as well as on a front coated mirror (attached to the sample at right angles) at an angle of θ with the sample surface-normal. The reflected beam interferes with the partially illuminating direct beam incident on the sample surface producing 1D periodic intensity distribution with periodicity given by $\Lambda=\lambda/(2\ \sin\theta)$. With optimization of the exposure dosage (i.e., exposure time) by the electronic shutter as well as the developing time, gratings etched up to the TIO_2 layer can be formed with an exposure time of 1 second and developing time of 20 seconds. Figure S3 (b) shows an AFM measurement of the produced grating pattern to reveal grating thickness around 150 nm etched up to the glass substrate which has been further confirmed by FIB cut as reported in the paper. Thus depending on the collimated beam size, about 1 cm^2 area of fabricated GMR structure can be obtained with uniformed patterning throughout the area.

T4: Directed self-assembly for the arrangement of particles

For the hybrid structure, synthesized plasmonic gold nanoparticles are required to be incorporated within the channels of the fabricated dielectric GMR structure. Due to spherical symmetry, concern about the final orientation of these nanoparticles relative to the channel does not arise. In the convective assembly experiment, 25 µL of gold nanoparticle solution (0.5 mg/mL, pH 9) is confined between the hydrophilized (30 s O_2-plasma, 0.2 mbar, 80 W, Flecto 10, Plasma Technology) topographical nano-channel substrate and a stationary glass slide (distance 0.5 mm). The substrate is withdrawn at a speed of 1 µm/sec to make the meniscus recede in the direction parallel to the channels. The evaporation, facilitated at the meniscus drives a convective flow of particles towards the contact line. On the well wetting substrate, the fluid spreads inside the channels due to the capillary pressure. The nanoparticles travel along the liquid-filled channels that create both lateral and vertical (liquid film thickness) confinement. As soon as the particles protrude from the liquid film upon drying, attractive capillary forces arise between the particles to guide the crystallization into dimer lines of particles (Figure S4).

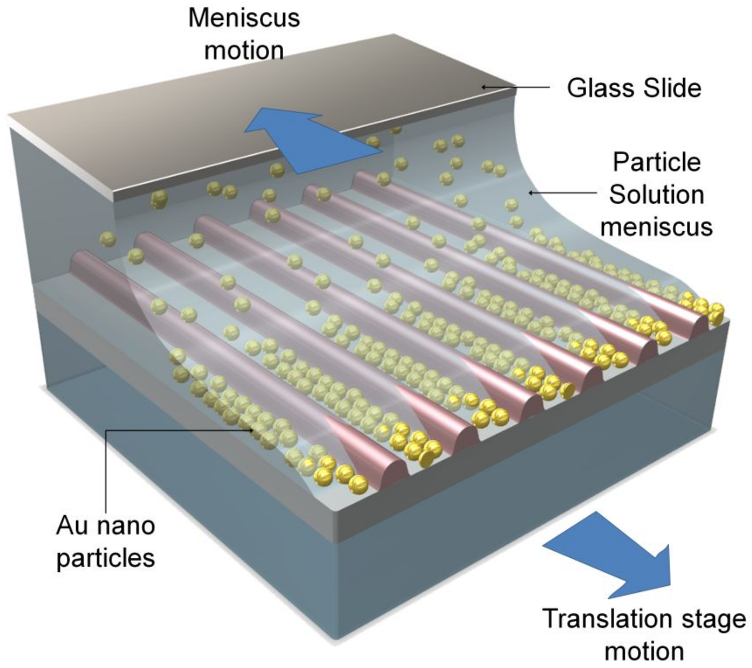

Figure S4 | Directed self-assembly of gold nanoparticles within grating channels of a dielectric GMR structure.

T5: Optical characteristics of the different resonant geometries in transverse magnetic (TM) mode.

In contrast to the optical characteristics of different resonant geometries under transverse electric (TE) polarization as studied in Figure 3 of the main article, the effect of the transverse magnetic (TM) polarization is also studied here for comparison. Figure S5 presents both experimental and simulative results of the plasmonic, photonic and hybrid structures for the similar scan range (0° to $\pm 30°$) as shown in Figure 3. Plasmonic bands (red) as obtained from the angle of incidence scan shows isolated particle features for the plasmonic chains around 530 nm (Figure S5 (a)) that can be seen from the transmittance spectra. For pure photonic GMR structure (Figure S5 (b)), the resonant modes (θ_{inc} = 0° and $\neq 0°$) doesn't lie within the spectral position of the plasmonic band. Thus the hybrid geometry (Figure S5 (c)) exhibits no such hybridization for the case of TM polarization.

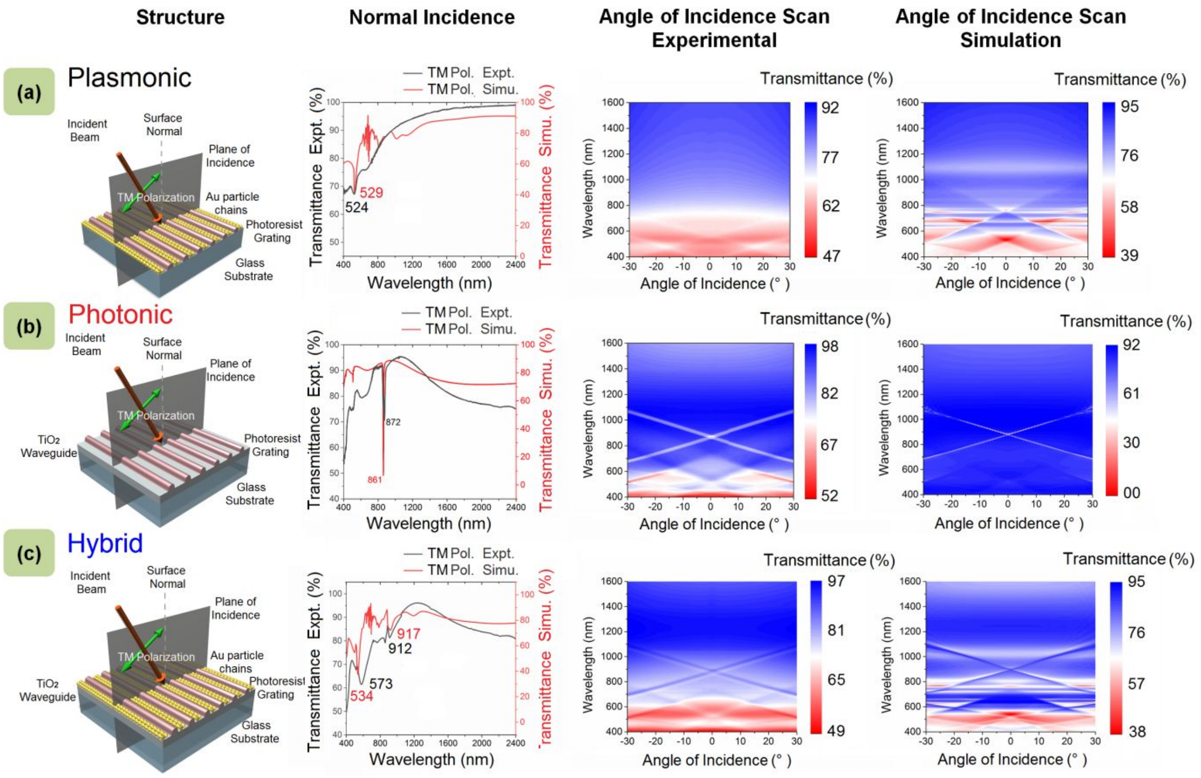

Figure S5 | Comparison of optical properties of three different structures in TM mode: (a) Plasmonic dimer lines of gold nanoparticles with 520 nm periodicity supported by photoresist gratings on a glass substrate. Both experiment and simulation studies show particle resonance around 530 nm for excitation with TM polarization across the chain directions. Variation of the incidence angle experimentally exhibits a constant dip supported by simulations. (b) A dielectric GMR structure with photoresist grating (of periodicity 520 nm and thickness 150 nm) on TiO_2 waveguide (of 200 nm thickness) and the glass substrate. Experimental studies observe transmission dip at 872 nm for normal incidence and similar dip at 861 nm for simulation with the splitting of modes on varying the angle of incidence. (c) A hybrid plasmonic-dielectric resonant structure with gold nanoparticle dimer lines filled within grating lines of a dielectric GMR. On normal incidence, particle modes are excited around 550 nm with guided waveguide modes at far separated higher wavelengths of around 915. Scanning of incidence angle reveals non-interaction of plasmonic mode with the photonic GMR modes angles as observed from both experimental and simulation data.

T6: Comparison of plasmonic bars with similar dimension in hybrid geometry

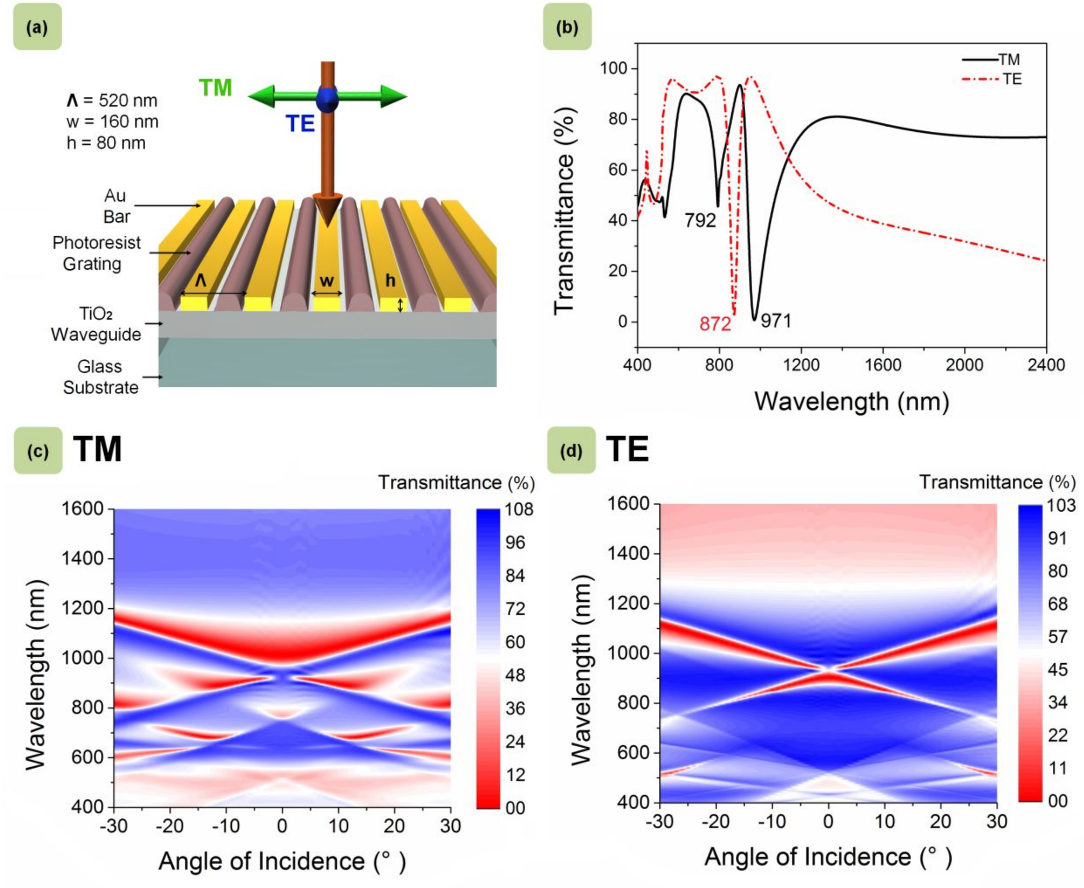

Figure S6 | Simulative study on optical properties of hybrid opto-plasmonic geometry with a grating of metallic gold bars: (a) Plasmonic gold nanograting with 520 nm periodicity, 160 nm width and 80 nm height along with photoresist grating on 200 nm thick TiO_2 waveguide layer. (b) Transmission spectra of the structure in TM and TE modes under normal incidence. Hybridized modes are obtained in TM polarization at 792 and 971 nm whereas sharp dip relating to GMR is obtained for the TE case. (c), (d) Angle of incidence (AOI) scan with TM and TE polarization respectively. TM mode shows signatures of hybridization similar to that in longitudinal excitation (TE) of plasmonic nanoparticle chains as discussed in the main article. TE mode shows prominent GMR properties of mode splitting with broadening of dips on increasing the AOI.

The plasmonic gratings of gold bars have been reported to show plasmonic features on exciting with polarization perpendicular to the grating lines (TM) whereas normal grating like behavior with parallel polarization (TE). When combined with a waveguide, the TM mode causes generation of waveguide-plasmon polaritons due to strong coupling whereas TE mode results only in the generation of photonic waveguide modes leading to GMR. We compare our hybrid geometry by replacing nanoparticle chains with nano bars where the height and width are kept identical in both cases (Figure S6 (a)). One can observe hybridization for the case of TM polarization (Figure S6 (b)) in case of metallic bars which is expected from literature. This is because, for TM polarization, the plasmonic band of the metallic bar is around 800 nm which can interact with the photonic GMR TM mode resulting in hybridization. For TE case, the photonic mode finds no plasmonic counterpart to interact and thus is devoid of any such coupling. The angle of incidence scan further confirms the outcome as seen from Figure S6 (c-d).

T7: Electric field plots at resonance for different cross-sections

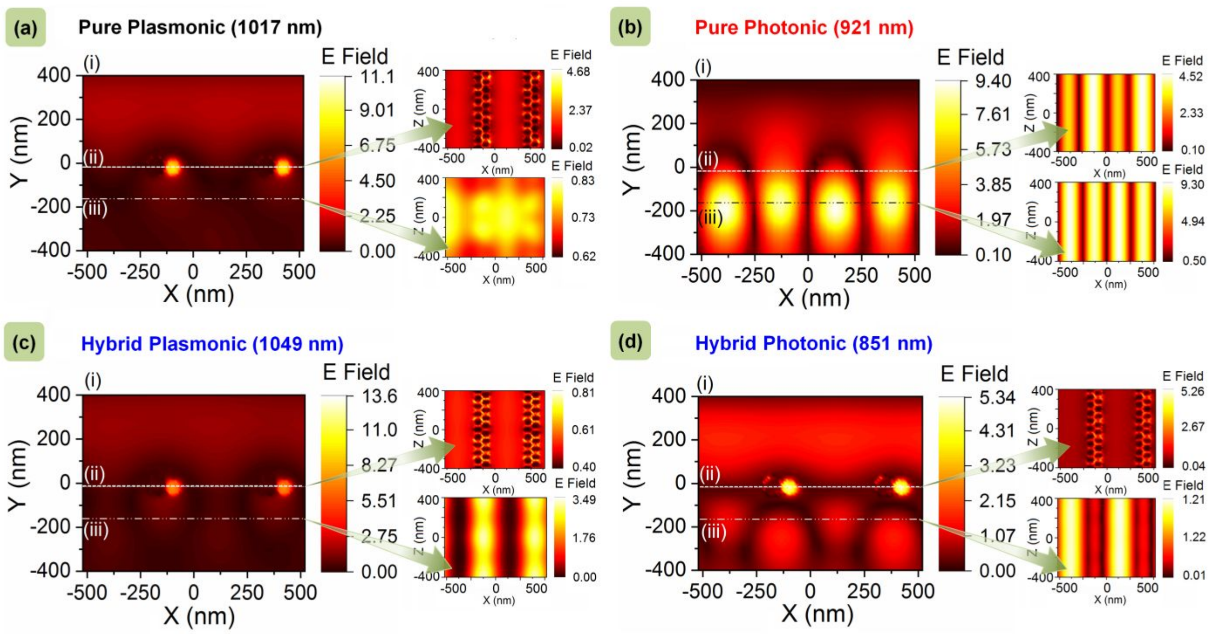

Figure S7 | Electric field distribution of pure and hybridized modes: (a-d) Electric field distributions for pure and hybrid geometry with monitors (i) across layers and (ii), (iii) within layers along particle and waveguide plane respectively. The pure resonant modes are excited by TE polarized source at 1017 nm (plasmonic) and 921 nm (photonic) whereas the hybrid ones at 1049 nm (plasmonic) and 851 nm (photonic).

Figure S7 (a-d) shows the electric field $\left(|\vec{E}|\right)$ distribution for pure and hybrid structures with 'frequency domain field profile' monitors in both XY (i) and XZ planes (ii: chain layer, iii: waveguide layer). On exciting the structures with corresponding resonant wavelength, the XY monitors (i) of Figure S7 (a, b) show field strength around the particles and in the waveguiding medium for cases of pure plasmonic and photonic respectively. For excitation of the hybrid structure with the two resonant frequencies, hybrid-plasmonic mode exhibits field enhancement surrounding the particles whereas the hybrid-photonic mode shows mode formation inside the waveguide along with excitations around the particles. From the XZ monitors (ii, iii) in Figure S7 (a, b), pure plasmonic and pure photonic modes show confinement along their characteristic systems i.e., the particle chains layers and the waveguiding layer respectively. Incorporating these features together in a hybrid structure provides mixed features in both the resonating states. Compared to pure plasmonic (Figure S7 (a, ii)), the hybrid plasmonic (Figure S7 (c, ii)) has similar features with photonic waveguide type features induced in (Figure S7 (c, iii)). However, the effect of plasmonic behavior is predominant and the modes are spatially oriented in accordance with the position of the plasmonic chains. The, hybrid photonic (Figure S7 (d, iii)) in comparison to pure photonic (Figure S7 (b, iii)) shows similar mode formation along the waveguiding layer with plasmonic like features in (Figure S7 (d, ii)) due to the influence of the particles. Thus it appears that due to mthe ixing of the geometries both the hybrid modes have characteristics of the pure states via hybridization. This is described in the main article through our hybridization model.

T8: Refractive index measurement for sensing

The refractive indices of pure water and salt solution as described in the main article are measured using a digital refractometer for five discrete wavelengths. Using Cauchy's dispersion equation, the coefficients B, C, and D are determined which are further used to extrapolate values of a real part of the refractive index (n) for the entire range of wavelength scan from 400-2400 nm. Figure S8 (a) and (b) show the 'n' values of pure water and salt solution respectively as a function of wavelength. These data are also incorporated within the simulation model to observe the sensitivity of different resonant structures on changing surrounding media from pure water to salt solution.

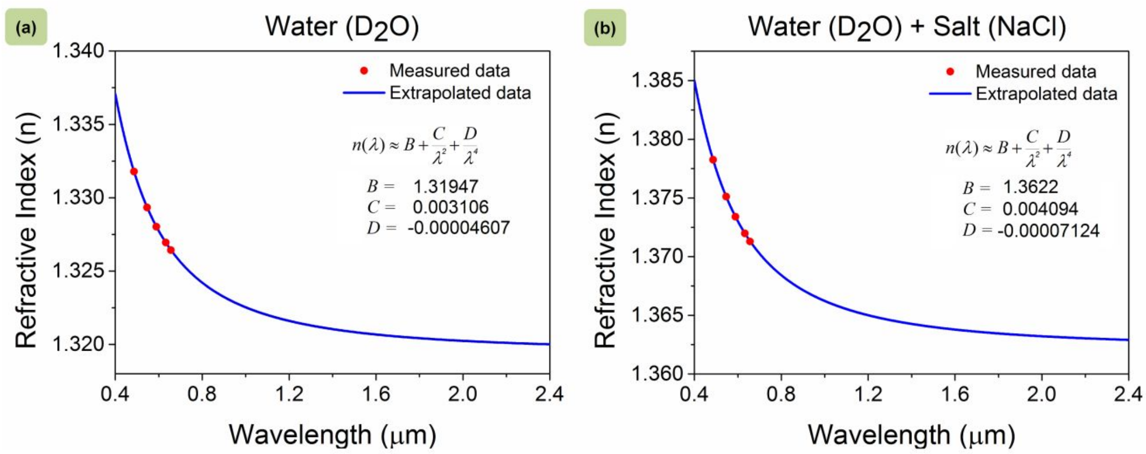

Figure S8 | Refractometer data: The real parts of refractive index (r. i.) are plotted for (a) heavy water (D_2O) and (b) salt solution (NaCl in D_2O, 0.3g/ml) using known values measured at five different wavelengths by a refractometer

T9: Spectra for sensing measurements with water as a cover medium

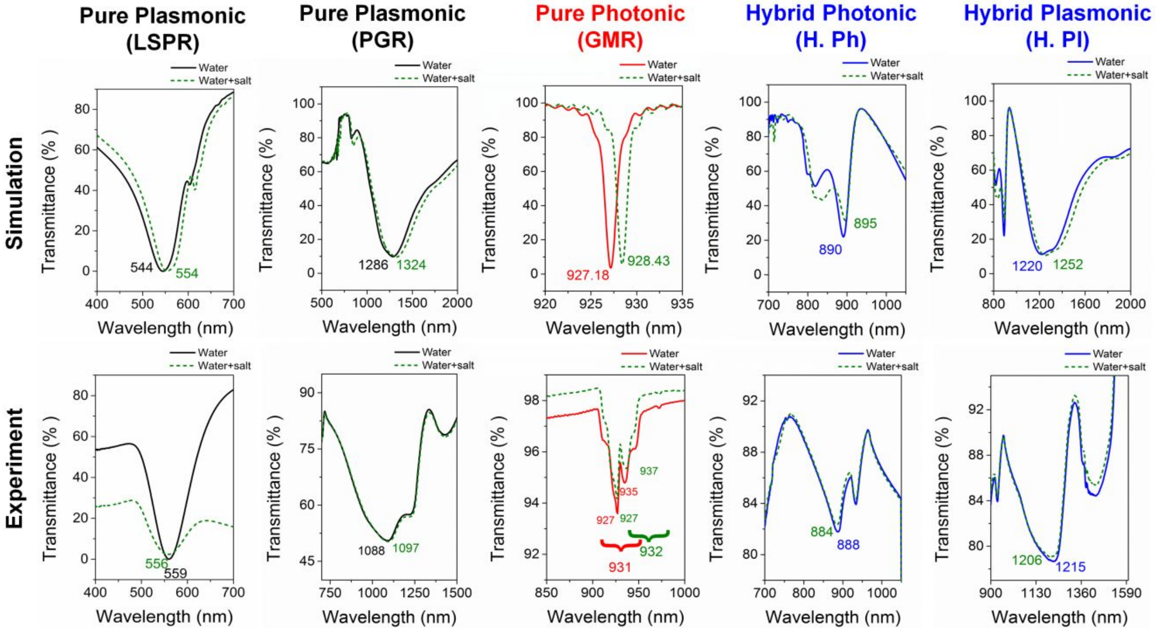

Figure S9 | Effect of cover index variation with water as a cover medium: Comparison of both simulation and experimental transmission spectra for geometries operating on different resonance regimes. Deuterium Oxide (D_2O) is chosen as a background medium whose refractive index (RI) is varied by mixing sodium chloride (NaCl). For simulation, such media are modeled using RI data given in Figure S8.

Figure S9 shows the simulation (simu.) as well as experimental (expt.) spectra for all the resonant mechanisms in water medium that are compared in the main article in terms of sensitivity and figure of merit. The results are compiled in Table S1.

Table S1 | Refractive index sensing with water: Calculation of sensitivity (S) and figure of merit (FOM) for different resonance geometries from the simulation as well as experimental transmission spectra plotted as a function of different refractive index in Figure S9. The values of the refractive indices at different resonant wavelengths for both the cases of pure water and salt solution are estimated from the Cauchy relation and coefficients given in Figure S8.

	Method	**λ_1 (nm)**	**n_1 (RIU)**	**FWHM 1 (nm)**	**λ_2 (nm)**	**n_2 (RIU)**	**FWHM 2 (nm)**	**Δn (RIU)**	**Δλ (nm)**	**FWHM Avg (nm)**	**S (nm/ RIU)**	**FOM (S/ FWHM)**
LSPR	***Simu.***	544	1.3294	88	554	1.3748	90	0.0454	10	89	220.26	2.47
	Expt.	559	1.3289	74	556	1.3747	66	0.0458	3	70	65.50	0.94
PGR	***Simu.***	1286	1.3213	449	1324	1.3645	474	0.0432	38	461.5	879.62	1.91
	Expt.	1088	1.3221	393	1097	1.3656	393	0.0435	11	393	252.87	0.64
GMR	***Simu.***	927.18	1.3230	1.52	928.43	1.3667	1.36	0.0437	1.25	1.44	28.60	19.86
	Expt.	931.0	1.3229	21.36	932.0	1.3668	23.19	0.0439	01	22.28	22.78	1.02
H. Ph.	***Simu.***	890	1.3233	114	895	1.3671	105	0.0438	05	109.5	114.16	1.04
	Expt.	888	1.3233	109	884	1.3673	111	0.044	04	110	90.9	0.82
H. Pl.	***Simu.***	1220	1.3215	406.5	1252	1.3648	440.5	0.0433	32	423.5	739.03	1.74
	Expt.	1215	1.3219	379	1206	1.3650	368	0.0431	09	373.5	208.81	0.56

T10: Spectra for sensing measurements with air as a cover medium

With air as a cover medium, sensitivity (S) and figure of merit (FOM) for different resonance geometries from FDTD simulation spectra for different regions of the resonating structures are investigated. In order to obtain sensitivity in the air, simulation background of the FDTD model is changed from 1.0 to 1.1 for all the resonance mechanisms (pure and hybrid) that have been previously studied under normal incidence for their transmittance over the span of 400-2400 nm. In addition, LSPR corresponding to isolated nanoparticle suspension is also studied theoretically. Due to the absence of any gaseous medium having index 1.1, the study is strictly confined to the case of simulation and corresponding spectra are presented in Figure S10 (a). Table S2 contains the tabulated values of S and FOM which shows similar trends for sensitivity in water as tabulated in Table S1 corresponding to the different resonance geometries.

Till now, all the sensing studies that have been performed via modeling are considered with material optical constants properly fed into the simulation model. For a quick theoretical comparison of sensitivity at different regions of the resonant structures, the effect of variation of waveguide and substrate indices are now included as a part of the sensitivity study to understand the effect of localization of pure and hybrid modes at different regions. For both the cases of waveguide and substrate index variation, the cover index is kept 1.0. While choosing waveguide as the layer of interest (LOI), its index is considered 2.1 for the entire spectral range which is increased to 2.2 to observe the effect of variation. Similarly, for the substrate as LOI, the index value is changed from 1.45 to 1.55. The results are plotted in Figure S10 (b) and (c) and compared with that in Figure S10 (a). The corresponding S and FOM values from the graph are calculated and also tabulated in Table S1 for comparison. Since the LSPR study contains no waveguide and substrate, it is excluded in Figure S10 (b) and (c). Likewise, the PGR study containing no waveguide is excluded in Figure S10 (b). The S and FOM values from Table S1 and S2 for all the resonant geometries are summarized as plots in Figure 5 for a quick analysis.

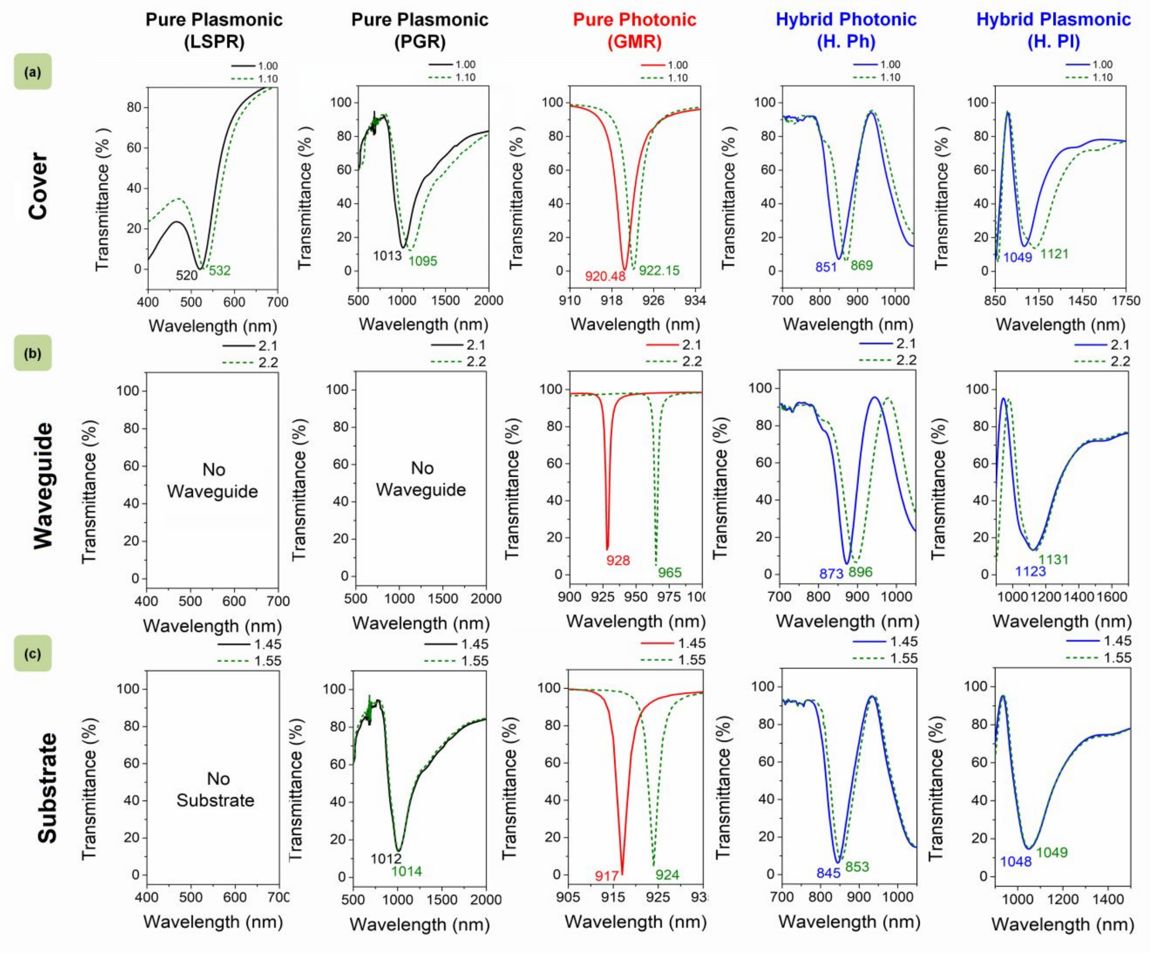

Figure S10 | Effect of index variation for different regions of the resonant structures: An FDTD evaluation. (a) Cover index changed from 1.0 to 1.1 that represents sensing performance of the resonant structures in the air. (b) Waveguide index varied from 2.1 to 2.2 for all of the associated structures with optical constants of the other constituting materials intact. (c) Substrate index varied from 1.45 to 1.55 for all the resonant geometries with other material indices fixed.

Table S2 | Effect of index variation: Calculation of sensitivity (S) and figure of merit (FOM) for different resonance geometries from FDTD simulation spectra for different regions of the resonating structures.

Layer of Interest	Resonance type	n_1 (RIU)	λ_1 (nm)	FWHM 1 (nm)	n_2 (RIU)	λ_2 (nm)	FWHM 2 (nm)	Δn (RIU)	Δλ (nm)	FWHM Avg (nm)	S (nm/ RIU)	FOM (S/ FWHM)
Cover	**LSPR**	1.0	520	41	1.1	532	45	0.1	12	43	120	2.79
	PGR		1013	330.4		1095	432		82	381.2	820	2.15
	GMR		920.48	3.67		922.15	2.97		1.67	3.32	16.7	5.03
	H. Ph.		851	67.2		869	51.39		18	59.3	180	3.04
	H. Pl.		1049	254.1		1121	167.7		32	210.9	320	1.52
Waveguide	**LSPR**	2.1	-	-	2.2	-	-	0.1	-	-	-	-
	PGR		-	-		-	-		-	-	-	-
	GMR		928	3.17		965	2.89		37	3.03	370	122.11
	H. Ph.		873	55.45		896	71.63		23	63.54	230	3.62
	H. Pl.		1123	267.67		1131	247.23		08	257.45	80	0.31
Substrate	**LSPR**	1.45	-	-	1.55	-	-	0.1	-	-	-	-
	PGR		1012	315.10		1014	324.11		02	319.61	20	0.06
	GMR		917	2.88		924	2.52		07	2.7	70	25.92
	H. Ph.		845	67.22		853	65.12		08	66.17	80	1.21
	H. Pl.		1048	187.26		1049	180.06		01	183.66	10	0.05